A strategy for preparation of Fe_2O_3/g-C_3N_4 composites with efficient visible-light photocatalytic activity

XUEWANG ZHU[a], XUEJIA TIAN [a], RONG YIN[a], QINGZHI LUO[a], JING AN[a], XUEYAN LI [a], DESONG WANG[a,b,*]
[a]*School of Sciences, Hebei University of Science and Technology, Shijiazhuang 050018, People's Republic of China*
[b]*Metastable Materials Science and Technology State Key Laboratory, Yanshan University, Qinhuangdao, 066004, People's Republic of China*

A new strategy was developed for preparing Fe_2O_3/graphitic carbon nitride (Fe_2O_3/g-C_3N_4) composites exhibiting greatly promoted photocatalytic active under the condition of visible light. Ferric chloride solution was added into melamine solution with pH value of 2.0 at 90 ℃, the solution was cooled to room temperature to prepare re-crystallized melamine containing a little Fe(III) compounds. The re-crystallized melamine underwent heating process at 550 ℃ for 2 h to prepare Fe_2O_3/g-C_3N_4 composites. The as-prepared composites were analyzed through XPS, XRD, SEM, FT-IR. The photocatalytic active condition of Fe_2O_3/g-C_3N_4 was researched by photodegradation of Rhodamine B as irradiated by visible light. The facilitated absorption of light and significant photo-generated electron and hole separation were realized through Fe_2O_3 loading. The photocatalytic activity of Fe_2O_3/g-C_3N_4 first increased and decreased as Fe_2O_3 content increased. The Fe_2O_3/g-C_3N_4 with Fe(III) compounds loading of 0.1 wt% exhibited the optimal photoactivity. The apparent rate constants of Fe_2O_3/g-C_3N_4 composites were almost 12.1 times than pure g-C_3N_4. The Fe_2O_3/g-C_3N_4 demonstrated noticeable stability and reusability.

(Received November 16, 2019; accepted October 22, 2020)

Keywords: Photocatalyst, Fe_2O_3, g-C_3N_4, Visible-light photocatalysis, Composites

1. Introduction

Over the last few decades, environmental pollution has become a serious problem worldwide. The direct solar energy conversion into chemical energy or organic pollutants mineralization through semiconductor photocatalysis mediated by sunlight-driven photoredox reactions have been regarded as long-term solutions for global energy and environmental problems. Semiconductor photocatalytic technology based on solar energy has been applied in numerous areas, including pollutant removal from water and air, hydrogen production, organic synthesis, and carbon dioxide reduction [1-7]. TiO_2 and ZnO photocatalysts have attracted the majority of research attention given their high chemical stability, nontoxicity, reusability, and low cost [8-10]. The large-scale applications of these photocatalysts, however, are limited by their disadvantages of low quantum efficiency, easy deactivation, and poor solar energy exploitation. Therefore, developing novel and efficient photocatalysts has become a crucial issue in the field of photocatalytic research.

Graphitic carbon nitride (g-C_3N_4) refers to a polymeric semiconductor using tri-s-triazine as the basic building unit. g-C_3N_4 tri-s-triazine units are connected by planar amino groups. g-C_3N_4 band gap is 2.7 eV, leading to visible-light absorption characteristics. Wang et. al. [11] calcined cyananmide to prepare g-C3N4 powder, which was then used in hydrogen development and photodegradation of organic contaminants as irradiated by visible light (λ > 420 nm) illumination. Yan et al. [12] synthesized g-C_3N_4 powder through giving heat to melamine under different temperature conditions and found that g-C_3N_4 powder produced at 520 ºC displayed the maximum photocatalytic degradation activity for methyl orange. g-C_3N_4 photocatalysts arouse considerable attention in the photocatalysis field of visible-light because of their nontoxicity, low price, and superior chemical stability [13-14].

Nevertheless, g-C_3N_4 can only absorb light shorter than 460 nm, its photogenerated electrons and holes recombine quickly. These drawbacks result in low g-C_3N_4 visible-light photocatalytic active condition and restrict its large-scale practical utilization. Therefore, the production of modified photocatalysts based on g-C_3N_4 with efficient photocatalytic activity has become a matter of urgency [15-17]. Some methods are employed for enhancing g-C_3N_4-based photocatalysts' catalytic efficiency and facilitating hole and photo-generated electron separation. These methods include doping of various elements [18-20], coupling two semiconductors [21-26], acid treatment [17, 28] and modifying with conjugated polymers [29, 30].

Fe_2O_3 has received considerable attention as a promising photocatalytic material because of its merits, such as environmental compatibility, low cost, and natural abundance. Fe(III) compounds could function as an effective electroncocatalyst that could improve the photocatalytic property of semiconductor materials in visible-light [31-33]. In reference to our previous work [34-36], we fabricated a novel composite by embedding Fe(III) compounds into g-C_3N_4 through a facile approach with ferric chloride, melamine as main reactants. We characterized the as-prepared Fe_2O_3/g-C_3N_4 photocatalysts through various instruments, and evaluated the as-prepared Fe_2O_3/g-C_3N_4 composite's photocatalytic activity in the photodegradation of Rhodamine B (RhB) solution under visible-light.

2. Experimental

2.1. Materials

Aladdin provided melamine. Ferric chloride, hydrochloric acid were from Tianjin Yongda Co, Ltd, China. Rhodamine B (RhB) was supplied by the development center of Tianjin kermel chemical reagent. All these chemicals were analytical pure and used directly. Water deionized was applied in the solution preparation process.

2.2. Photocatalyst production

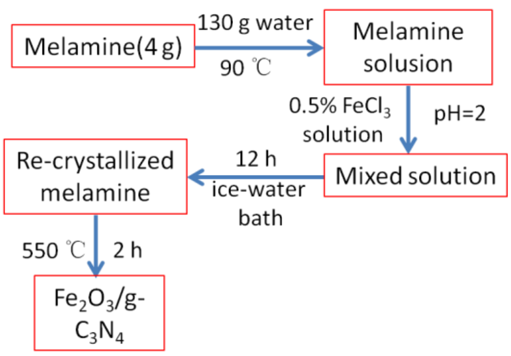

Scheme 1. The idealized preparation process of Fe_2O_3/g-C_3N_4 composites (color online)

With reference to the literatures [11, 37], clean g-C_3N_4 and v/g-C_3N_4 composites exhibiting various Fe_2O_3 amounts were prepared. Scheme 1 presents the idealized preparation process. The detailed description of the process is shown in **S1**.

2.3. Characterizations

Clean g- C_3N_4 and Fe_2O_3/g-C_3N_4 composites were studied by a variety of instruments as shown in **S2**.

2.4. Photocatalytic activity measurement

Through Rhodamine B photodegradation as irradiated by visible light, we assessed pure g-C_3N_4 and Fe_2O_3/g-C_3N_4's photocatalytic activity, as shown in **S3**.

3. Results and discussion

3.1. Characterizations of Fe_2O_3/g-C_3N_4

3.1.1 XRD

Fig. 1 gives XRD patterns of pure Fe_2O_3, pure g-C_3N_4, Fe_2O_3/g-C_3N_4 composite photocatalysts. Clean g- C_3N_4's XRD pattern shows 2 obvious peaks of diffraction at 27.7° and 13.1°, belonging to graphitic C_3N_4's hexagonal phase (JCPDS 87-1526). 27.7° peak belonging to g- C_3N_4 (002) plane [38] is because of the conjugated aromatic system's interlayer stacking, and 13.1°peak belonging to g- C_3N_4 (100) plane relates to an in-plane structural packing motif.

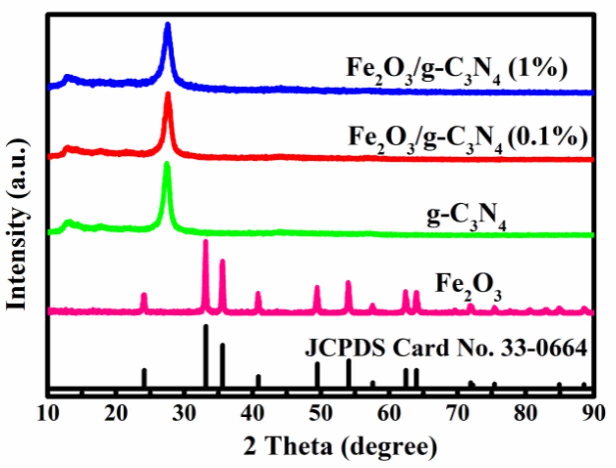

Fig. 1. XRD patterns of clean Fe_2O_3, pure g-C_3N_4, and Fe_2O_3/g-C_3N_4 composites (color online)

The mentioned 2 peaks of diffraction well comply with those previously found in [39]. Clean Fe_2O_3's XRD spectrum, the peaks at 24.18°, 33.15°, 35.75°, 40.93°, 49.43°, 54.02°, 57.56°, 62.51°, and 64.05° are attributed to the (012), (104), (110), (113), (024), (116), (018), (214) and (300) planes of hexagonal α- Fe_2O_3 (JCPDS No.33-0664), respectively. In Fe_2O_3/g- C_3N_4 composite photocatalysts' XRD spectrum, the two g- C_3N_4 characteristic peaks are texted, whereas those of Fe_2O_3 are not detected because it is present at low levels in the composites.

3.1.2. FT-IR

Fig. 2 shows clean g- C_3N_4, pure Fe_2O_3, and Fe_2O_3/g- C_3N_4 composites' FTIR spectra displaying various Fe_2O_3 loadings. The peak at 810 cm−1 in the spectrum of clean g- C_3N_4 is the characteristic peak of the triazine ring's bending vibration [40]. 1239, 1320, 1411, 1546, and 1639 cm−1 peaks belong to CN heterocyclic compounds' stretching vibration [41]. The peaks at 3000–3300 cm−1 are the N–H band's and O–H group's characteristic peaks in the water adsorbed in a physical manner on the catalyst surface [42-44]. The peaks at 469 and 566 cm−1 in pure Fe_2O_3 spectrum correspond to the Fe–O bond in Fe_2O_3. The emergence of peaks at 469, 566, 810, 1235–1640, and 3000–3300 cm−1 in the spectra of Fe_2O_3/g- C_3N_4 (0.1%) and Fe_2O_3/g- C_3N_4 (1%) reveals that Fe_2O_3 and g- C_3N_4 exist in Fe_2O_3/g- C_3N_4 composites. The slight shifts in the peaks at 812, 1238, 1316, 1407, 1542, and 1637 cm−1 in Fe_2O_3/g- C_3N_4 composite spectrum relative to those in pure g- C_3N_4 spectrum provide evidence for the robust Fe_2O_3 and g- C_3N_4 interaction.

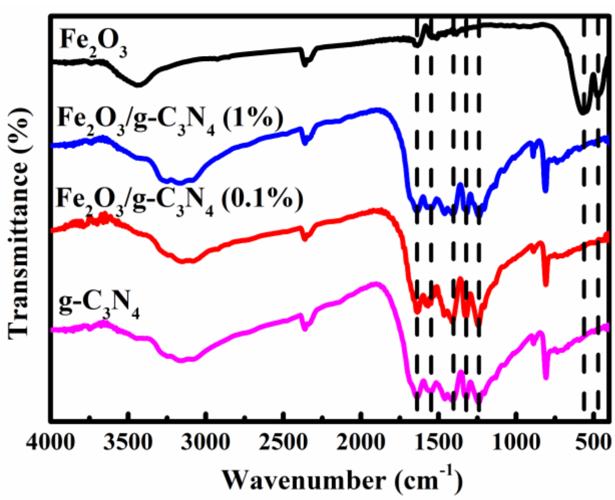

Fig. 2. FTIR spectra of clean g-C_3N_4, pure Fe_2O_3, and Fe_2O_3/g-C_3N_4 composites (color online)

3.1.3. XPS

Fig. 3 shows clean g- C_3N_4 and Fe_2O_3/g- C_3N_4 (0.1%)'s XPS survey spectra. The spectrum decomposition was performed using the XPS PEAK 4.1 program with Gaussian functions after subtraction of a Shirley background. Elements of C, N, and O are able to be identified in pure g- C_3N_4 XPS spectrum (Fig. 3[a]), whereas elemental C, N, O, and Fe are able to be observed in the XPS spectrum of Fe_2O_3/g- C_3N_4 (0.1%) (Fig. 3[b]). Elemental C and N originate from g- C_3N_4, whereas elemental Fe is derived from Fe_2O_3. Elemental O is contributed by Fe_2O_3 and the environment. C atom XPS spectrum (Fig. 3[c]) has 2 peaks at 287.8 and 284.6 eV belonging to N=C–N coordination and defects that contain sp2-hybridized C atoms in graphitic areas. The XPS spectrum of N atom (Fig. 3[d]) is divided into 3 peaks at 398.2, 399.0, and 400.4 eV. 400.4 eV peak belongs to C–NHX. The other two peaks belong to sp2-hybridized nitrogen (C=N–C) [39] and sp3-hybridized nitrogen (C–[N]3). The high-resolution XPS spectrum (Fig. 3(e)) of Fe 2p shows a representative Fe_2O_3 level with peaks at approximately 724.4 and 710.6 eV representing the Fe 2p1/2 and Fe 2p2/3 states [45, 46], separately. The XPS of the O atom spectrum displays 2 peaks at 533.4 and 531.9 eV [39]. The peak at 533.4 eV originates from H2O in the environment and that at 531.9 eV can belong to Fe–O of Fe_2O_3. Our FT-IR and XPS results confirm the formation of Fe_2O_3 in Fe_2O_3/g- C_3N_4 composites.

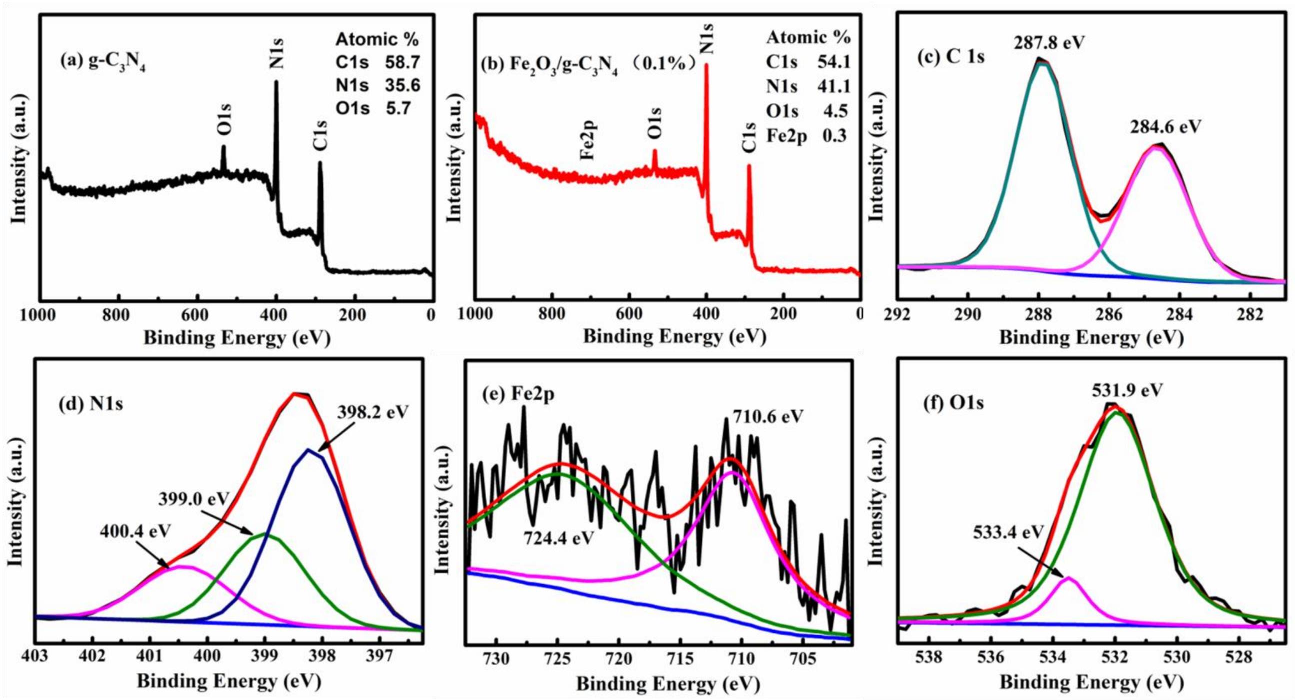

Fig. 3. XPS spectra of clean g-C_3N_4(a) and Fe_2O_3/g-C_3N_4(0.1%) (b) and C 1s(c), N 1s(d), Fe 2p(e), and O 1s(f) spectra of Fe_2O_3/g-C_3N_4(0.1%) (color online)

3.1.4. SEM and BET

The morphologies of g- C_3N_4, Fe_2O_3/g-C_3N_4(0.1%) had been obtained by SEM. As shown in Fig.4 (a) and (c), the particulates form of pure g-C_3N_4 and Fe_2O_3/g-C_3N_4 (0.1%) are similar, all of them have irregular shapes and sizes of approximately 0.5–1.5 µm. Fig. 4 (b) and (d) indicate that the surface of Fe_2O_3/g-C_3N_4 (0.1%) is rougher than that of g-C_3N_4 because Fe_2O_3 addition drastically changed g-C_3N_4 surface morphology. This is consistent with BET results (Fig. S1). The BET specific surface areas of pure g-C_3N_4 and Fe_2O_3/g- C_3N_4 (0.1%) are 8.6 and 27.0 m2/g, respectively. These results show that Fe_2O_3 addition can increase the specific surface area of pure g- C_3N_4 because of rougher surface, and the improvement of the photocatalyst's surface area favors the photocatalytic activity of g- C_3N_4.

The elemental mapping images are shown in Fig. S2. All elements are well-dispersed into the composite. These images indicate Fe_2O_3 and g- C_3N_4 are uniformly distributed in the composites.

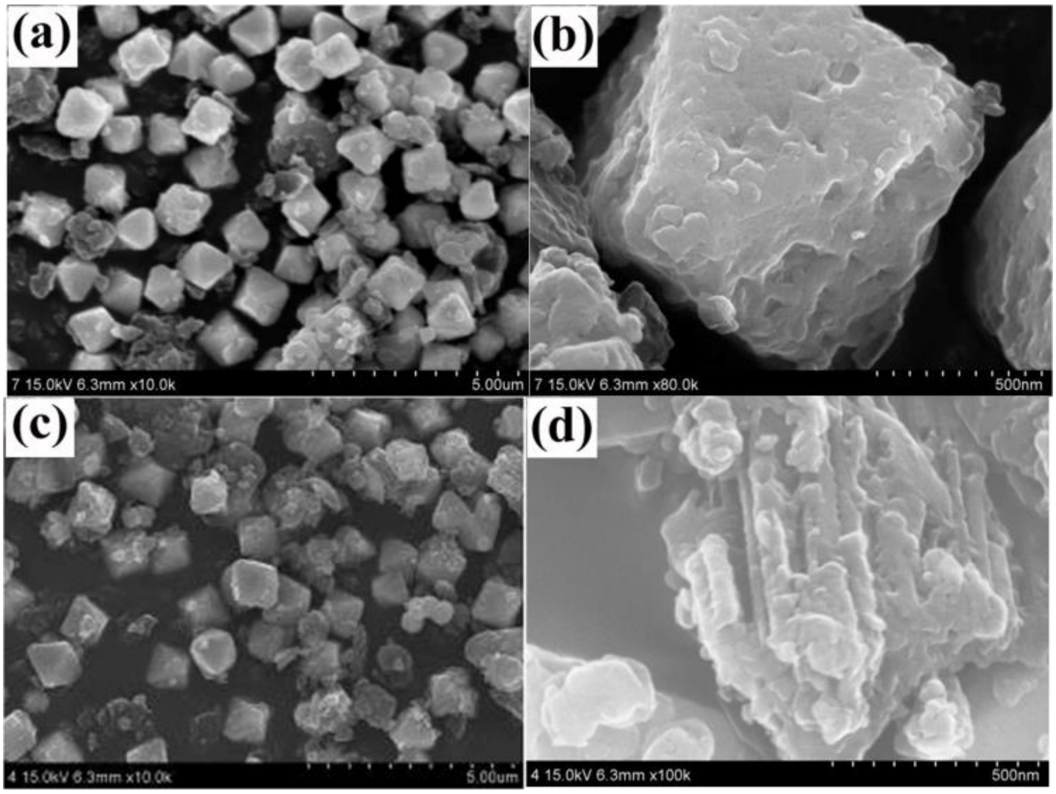

Fig. 4. SEM images of pure g-C_3N_4 (a, b) and Fe Fe_2O_3/g-C_3N_4(0.1%) (c, d)

3.1.5. DRS

Fig. 5 shows g-C3N4, Fe_2O_3/g-C3N4 composites' UV-Vis DRS. Fe_2O_3/g-C3N4 composites' light absorbance is higher than that of clean g-C3N4 in the ultraviolet light range of 250–400 nm and slightly increased under the visible light ranging from 400 to 800 nm. The intensity of absorbance is enhanced with the increment in the Fe_2O_3 content of the composite. Fe_2O_3/g-C3N4(0.1%) exhibits the maximal absorption intensity.

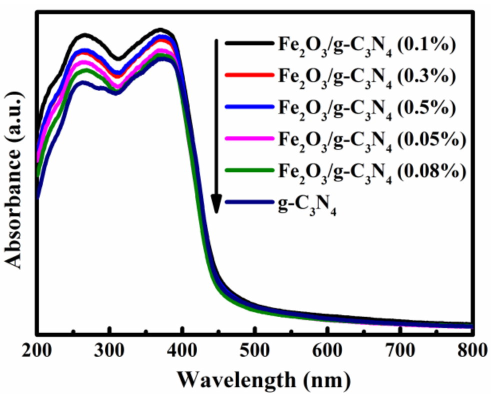

Fig. 5. UV-Vis DRS of g-C_3N_4 and Fe_2O_3/g-C_3N_4 composites (color online)

3.1.6. PL and EIS

Fig. 6 shows clean g-C3N4 and Fe_2O_3/g-C3N4 composites' PL spectra. PL measurements are critical to the investigation of the separation efficiency of the photon-generated carriers of semiconductors [47]. Fig. 6 shows that pure g-C3N4 possesses high fluorescence intensity, revealing the high recombination ratio of photon-generated carriers in the surfaces of g- C_3N_4. Adding trace amounts of Fe_2O_3 has drastically reduced the PL intensity of Fe_2O_3/g- C_3N_4 composites. The PL intensity of Fe_2O_3/g- C_3N_4 composites further decrease with the increment in Fe_2O_3 content. This result indicates that the efficiency of photogenerated electron-hole separation in Fe_2O_3/g- C_3N_4 composites has been enhanced, and the presence of Fe_2O_3 in the composites improves the separation efficiency of electrons and holes photo-generated.

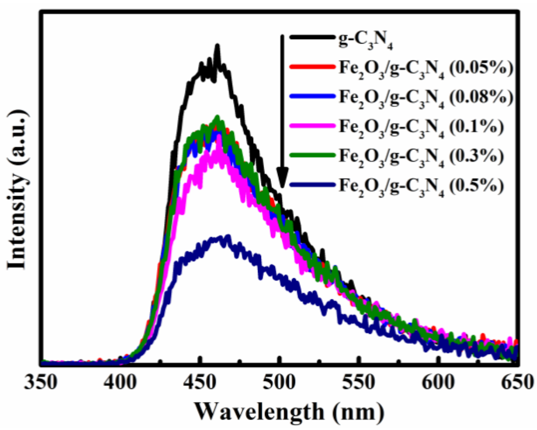

Fig. 6. PL spectra of clean g-C_3N_4 and Fe_2O_3/g-C_3N_4 (color online)

The result of EIS (Fig. S3) also illustrates this point [48]. The charge transfer rate on electrode surfaces is reflected by the the EIS Nyquist plots' arc radius. The arc radius of the EIS Nynquist plots of FTO/Fe Fe_2O_3/g-C_3N_4(0.1%) electrode is below FTO/g-C_3N_4 electrode's. This result further confirms the enhancement of the charge separation efficiency of Fe_2O_3/g-C_3N_4.

3.2. Visible-light photocatalytic performances of Fe_2O_3/g-C_3N_4 composites

The as-prepared pure g-C_3N_4 and Fe_2O_3/g-C_3N_4 composites' photocatalytic activity in RhB photodegradation under visible-light irradiation were quantified. As depicted in Fig. 7, RhB photodegradation rate in the presence of Fe_2O_3/g-C_3N_4 composites is higher than that in the presence of pure g-C_3N_4. As Fe_2O_3 content rises, the visible-light photocatalytic activity of Fe_2O_3/g-C_3N_4 composites first rises and then decreases. Fe_2O_3/g-C_3N_4 (0.1%) shows the highest photocatalytic activity under visible light. The association between ln(c_0/c) and irradiation time is shown in Fig. 8, indicating that the kinetics of RhB photodecomposition on the surfaces of the investigated photocatalysts can be described as a first-order reaction [49]. The apparent rate constant of RhB degradation over Fe_2O_3/g-C_3N_4 (2.70 h^{-1}) is more than 12.1 times that of clean g-C_3N_4 (0.222 h^{-1}). This result shows that the addition of a small amount of Fe_2O_3 can greatly improve the g-C_3N_4 composite's photocatalytic activity under visible light.

Stability is another vital factor that affects the photocatalytic activity of composites besides photocatalytic efficiency. For assessing the photocatalytic stability of Fe_2O_3/g-C_3N_4 (0.1 %) in the cycled photodegradation of RhB under visible light, a six-run test was performed. As shown in Fig. 9, the photocatalytic efficiency of the Fe_2O_3/g-C_3N_4 (0.1%) composite is only slightly reduced after six cycles. This result indicates that Fe_2O_3/g-C_3N_4 composites have good photocatalytic stability as irradiated by visible light.

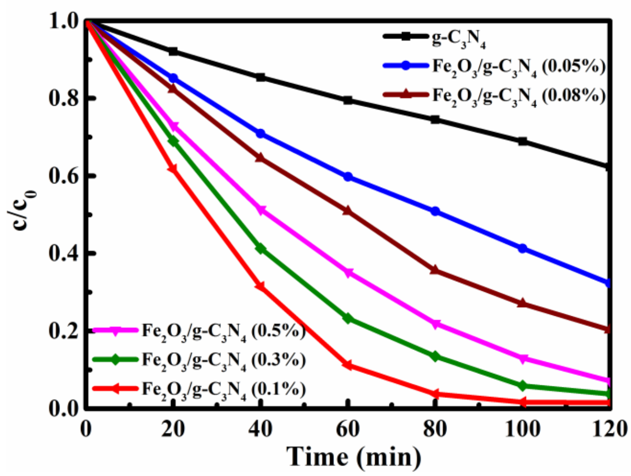

Fig. 7. RhB photodegradation when pure g-C_3N_4 and Fe_2O_3/g-C_3N_4 composites are present under visible-light irradiation (color online)

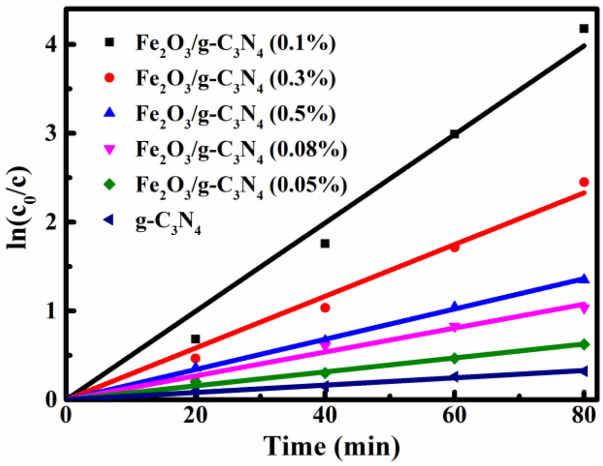

Fig. 8. Associations between ln(c_0/c) and photodegradation time when pure g-C_3N_4 and Fe_2O_3/g-C_3N_4 composites are present as irradiated by visible light (color online)

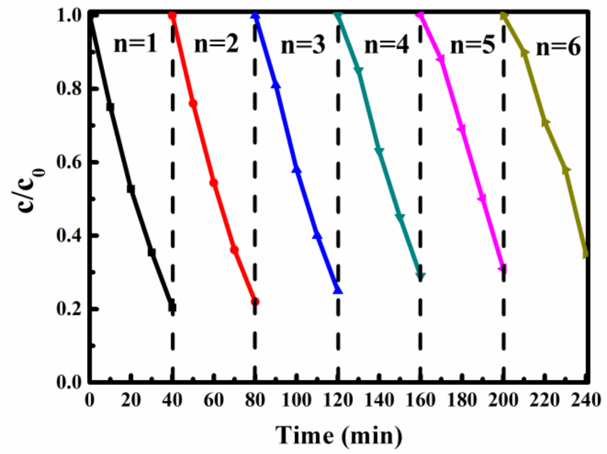

Fig. 9. Influence of the number of recycling runs on $Fe_2O_3/g\text{-}C_3N_4$ (0.1%)'s photocatalytic activity in RhB degradation as irradiated by visible light (color online)

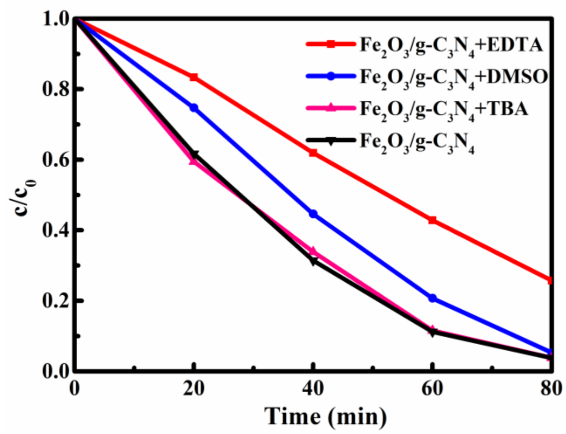

Fig. 10. Effects of EDTA, DMSO, and TBA on RhB photodegradation catalyzed by $Fe_2O_3/g\text{-}C_3N_4$(0.1%) under visible-light irradiation (color online)

A reactive species trapping experiment was performed to study the photodegradative mechanism of the composites. The influences of terephthalic acid disodium salt (TBA, a representative hydroxyl radical scavenger [49]), ethylene diamine tetraacetic acid (EDTA, a representative hole scavenger [50]), and dimethyl sulfoxide (DMSO, a representative electron scavenger [51]) on RhB photodegradation in the presence of Fe2O3/g- C_3N_4 (0.1%) were investigated, and the results are shown in Fig. 10. Both EDTA and DMSO significantly influence the photocatalytic degradation of RhB, and the effect of EDTA on the RhB photodegradation is more than that of DMSO. According to the mentioned result, electrons and holes photo-generated are the major active species responsible for Fe_2O_3/g- C_3N_4 (0.1%)'s photocatalytic activity.

3.3. Influencing factors of RhB photodegradation

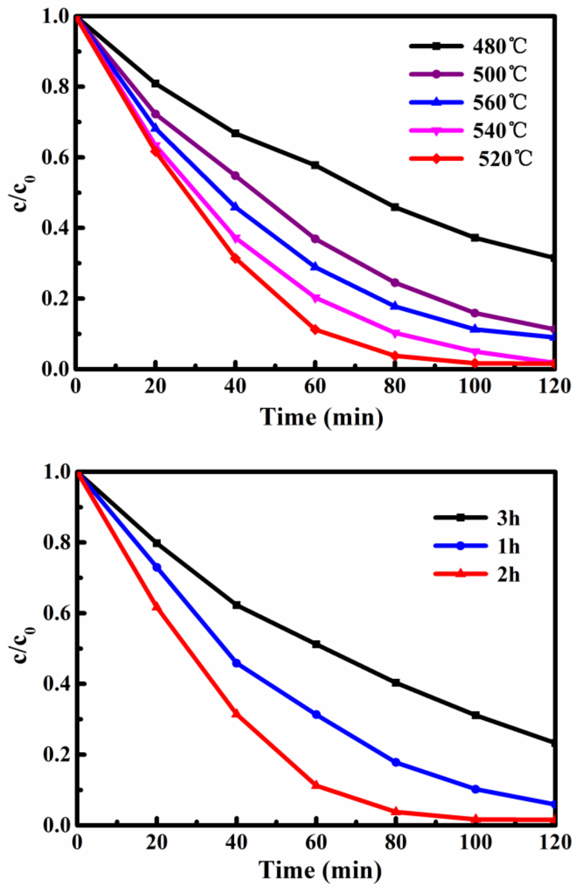

Fig. 11. Effects of heating temperature and duration on RhB photodegradation when $Fe_2O_3/g\text{-}C_3N_4$ (0.1%) is present (color online)

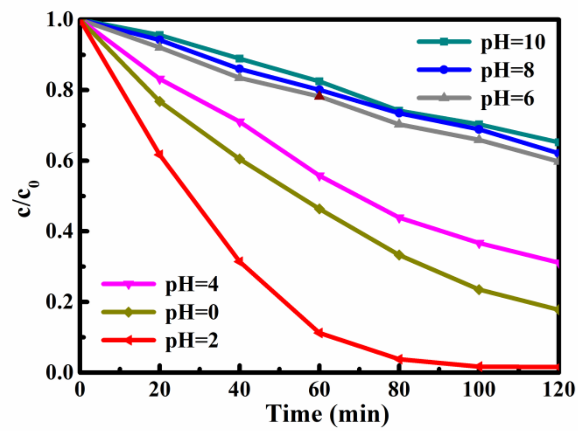

Fig. 12. Influence of the pH value on the RhB photodegradation rates (color online)

Heating temperature and time during fabrication greatly affect Fe_2O_3/g- C_3N_4 composites' photocatalytic activity in the case of visible light, and Fig. 11 presents the results achieved rom the experiment. As heating temperature and time rise, RhB photodegradation rate first rises and subsequently declines, and reaches the maximum value at the heating temperature and time of 520 ℃–540 ℃ and 2 h, respectively. Given this result, the optimal heating temperature and time for the preparation of Fe_2O_3/g- C_3N_4 composites are 520 ℃–540 ℃ and 2 h, respectively.

The effect of reaction suspension pH on RhB photodegradation rate is shown in Fig. 12. Similar to heating temperature and time, the pH value of the reaction suspensions obviously affects the RhB photodegradation rates. The RhB photodegradation rate first increases then decreases, and reaches the maximum value when the reaction suspension has a pH value of 2.

3.4. Visible-light photocatalytic mechanism of Fe_2O_3/g- C_3N_4 composites

Fig. 13 shows the proposed potential mechanism underlying Fe2O3/g- C_3N_4 composites' high photocatalytic activity in RhB degradation. Given that g-C_3N_4 has 2.7 eV band gap, capable of efficiently absorbing visible-light and being activated to holes and photo-generated electrons [52]. Fe(III) can easily oxidize photogenerated electrons to form Fe(II). Fe(II) has low stability, and it is easy to transform into Fe(III) through oxygen multielectron reduction in ambient cases ($4Fe^{2+} + O_2 + 4H^+ \rightarrow 4Fe^{3+} + 2H_2O$ or $4Fe^{2+} + O_2 + 2H_2O \rightarrow 4Fe^{3+} + 2OH-$) because the potential of Fe^{3+}/Fe^{2+} (0.771 V, vs SHE) is more positive than that of oxygen single-electron reducing process (O_2 + e- + H^+ → H_2O [aq], −0.046 V vs. SHE). Thus, Fe(III) can be recovered at high rates through the significant Fe(II) oxidation by oxygen [32,33].

This effect can enable the rapid photo-generated hole and electrons separation in Fe_2O_3/g-C_3N_4 composites. Such separation, in turn, promotes photocatalytic activity in the case of visible light. The major reactions can be illustrated below:

$$\text{g-C}_3\text{N}_4 + hv \rightarrow \text{g-C}_3\text{N}_4{*}$$

$$\text{g-C}_3\text{N}_4{*} \rightarrow \text{g-C}_3\text{N}_4(\text{e}^- e^- / h^+ h^+)$$

$$h^+ + RhB \rightarrow Degradation\ \ products$$

$$Fe^{3+} + e^- \rightarrow Fe^{2+}$$

$$Fe^{2+} + O_2 \rightarrow {}^{\bullet}\, O_2^{\,-} + Fe^{3+}$$

$${}^{\bullet}O_2^{\,-} + RhB \rightarrow CO_2 + H_2O$$

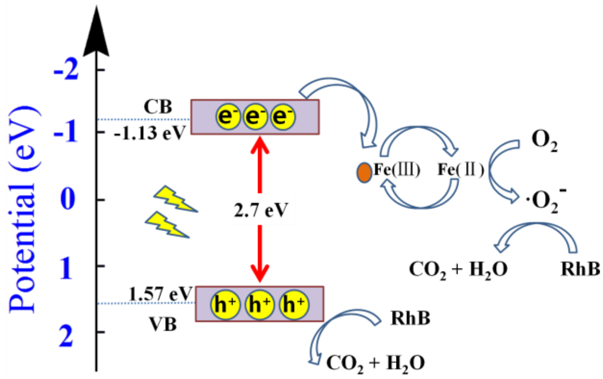

Fig. 13. Possible mechanism underlying Fe_2O_3/g-C_3N_4's the photocatalytic activity in the case of visible light (color online)

4. Conclusions

A novel and easy approach to fabricate Fe_2O_3/g-C_3N_4 composites using colloidal $Fe(OH)_3$/melamine as a precursor was presented. The low particulate Fe_2O_3 content of g-C_3N_4 improves absorbance under visible-light and hole/photogenerated electron separation efficiency while negligibly changing the crystallinity and size of g-C_3N_4. Fe_2O_3/g-C_3N_4 composites' visible-light photocatalytic activity is considerably larger than that of clean g-C_3N_4.The visible-light photocatalytic activity of the composites first rises and then decreases with increasing Fe_2O_3 content. Fe_2O_3/g-C_3N_4 (0.1%) displays the maximum visible-light photocatalytic activity. The results of recycling experiments further confirm that Fe_2O_3/g-C_3N_4 composites are highly stable. Therefore, our proposed approach, which involves the modification of g-C_3N_4 with less Fe_2O_3, represents an easy approach to prepare a visible-light photocatalyst.

Acknowledgements

This work was supported by the National Natural Science Foundation of China (No. 21271061), the Natural Science Foundation of Hebei Province (No. B2014208103, No. E2015208030) and the Key Basic Research Program of Hebei Province (No. 15961401D).

Associated content – Supporting information

S1 Photocatalyst preparation

In a typical preparation process, 4 g of melamine was firstly heated in a muffle furnace from room temperature to 550 ºC with a heating rate of 2 ºC min^{-1}. After heating at 550 ºC for 2 h, the as-prepared g-C_3N_4 was naturally cooled down to room temperature, and then the obtained yellow agglomerates were milled into powder in an agate mortar for further use.

The preparation of Fe(III)/g-C_3N_4 composites is described as follows. Firstly, 4.000 g of melamine was dissolved into 130.0 g of deionized water to form a solution at 90 ºC. Secondly, the above-obtained solution was adjusted to the pH value of 2, then a small amount of 0.5% $FeCl_3$ solution was added dropwise into the above solution under vigorous magnetic stirring for 15 min. After another 1 h stirring at 90 ºC, the resultant mixture solution was aged in an ice water bath for 12 h to produce re-crystallized melamine, and then the suspension was filtered, washed with deionized water for 3 times, and dried at 60 ºC for 5 h to obtain melamine containing iron compounds. Finally, the dried mixture was heated in the same way for preparing g-C3N4 to form Fe(III)/g-C_3N_4 composites. The as-prepared Fe(III)/g-C_3N_4 composites with different Fe_2O_3 contents were designated as Fe2O3/g-C3N4 (x%), where x % is the content of Fe_2O_3 in the Fe(III)/g-C_3N_4 composites. Pure Fe2O3 was prepared according to the above method in the absence of melamine.

S2 Characterizations

The crystal structure of the Fe(III)/g-C_3N_4 composites and pure g-C_3N_4 was investigated by X-ray diffraction (XRD) (Rigaku D/MAX-2500 diffractometer) in the range of 2θ from 5° to 100° using Cu Ka radiation (λ=0.15406 nm) with a Nickel filter as X-ray source. The accelerating voltage and applied current were 40 kV and 100 mA, respectively. Fourier-transform infrared spectra (FTIR) of the samples were determined on a Prestige-21 spectrometer (Shimadzu Co., Japan) in the range of 400-4000 cm^{-1} with standard KBr crystal salt tablets as the background. UV-Vis diffuse reflectance spectra (DRS) was performed on a SHIMADZU-2550 Scan UV-Vis system equipped with an integrating sphere attachment (Shimadzu Co., Japan) in the range of 200-800 nm, and $BaSO_4$ was used as the background. The photoluminescence emission spectra (PL) of samples were detected by a Fluorescence spectrophotometer (FS5-TCSPC., United Kingdom) at room temperature. XPS measurements were performed using a PHI 5000C ESCA system with Al Ka radiation (hv = 1486.6 eV) at a detection angle of 54°. The X-ray anode was run at 250 W, and the high voltage was kept at 15.0 kV. The emission SEM was performed using a HITACHI S-4800-I emission scanning electron microscope operated at accelerating voltage of 10 kV. Electrochemical impedance spectra (EIS) were measured by an electrochemical system (CHI 660E) which was using 0.1 M KCl solution as the electrolyte, platinum electrode as counter electrode, saturated calomel electrode (SCE) as reference electrode, and FTO/(Fe(III)/g-C_3N_4) or FTO/g-C_3N_4 electrode as the working electrode. Fe(III)/g-C_3N_4 and g-C_3N_4 films were coated by a doctor-blade method on the FTO substrates (fluorine-doped SnO_2, 15X/sq). The Brunauer-Emmett-Teller (BET) surface area measurements were performed using a Micromeritics TriStar II 3020 surface area and porosity system using nitrogen as adsorption gas at 77 K.

S3 Photocatalytic activity measurement

The photodegradation of RhB was used to evaluate the visible-light photocatalytic activity of the Fe(III)/g-C_3N_4 composites and pure g-C_3N_4. The investigated photocatalysts (0.10 g) were added into a cylindrical glass vessel containing an aqueous RhB solution (100 mL, 4 M), and the obtained suspension was continuously stirred in the dark for 1 h in order to reach an adsorption-desorption equilibrium before irradiation. Then, the suspension was irradiated under the visible light emitted from a 300 W iodine tungsten lamp (Philips Co.) with a 400 nm optical filter. The distance between the surface of the suspension and the light source was about 45 cm. During irradiation, the samples were taken out every 20 min from the reactor, and were centrifuged to separate the solid photocatalysts. The clarified solution was analyzed by a 723 UV-vis spectrometer (Shanghai Spectrum Instruments Co., Ltd., China), and the absorbance of RhB was measured at a wavelength of 554 nm, corresponding to the maximum absorbance wavelength of RhB solution at natural pH conditions. The concentration of RhB solution was obtained by a calibration curve. The symbols of c_0 and c are the concentrations of RhB before and after photoirradiation, respectively.

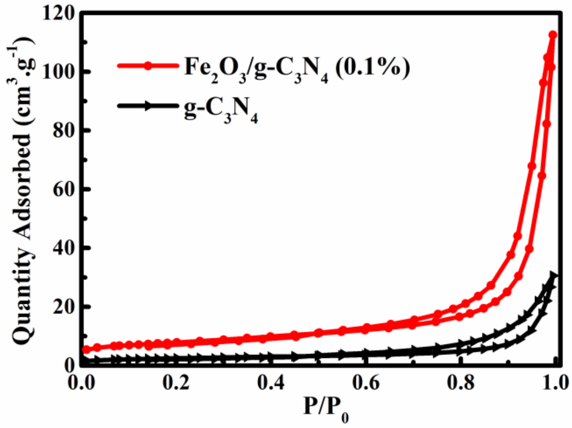

Fig. S1. N_2 adsorption-desorption isotherms of pure g-C_3N_4 and Fe(Ⅲ)/g-C_3N_4 (0.1 %) (color online)

The N_2 adsorption–desorption isotherms of pure g-C_3N_4 and Fe(Ⅲ)/g-C_3N_4(0.1%) are shown in Fig. S1. Both photocatalysts show type-I isotherm with H3 hysteresis loops. The formation of H3 hysteresis loops may be attributed to the aggregation of plate-like particles.

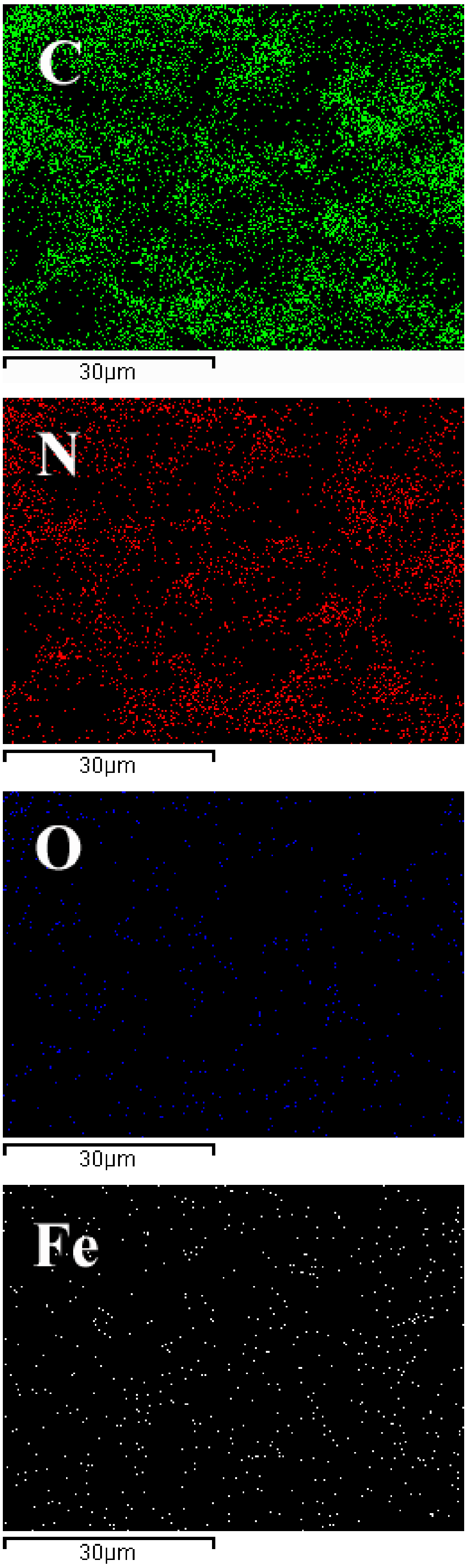

Fig. S2. Elemental mapping images of C, N, O, and Fe in Fe(Ⅲ)/g-C_3N_4(0.1%) (color online)

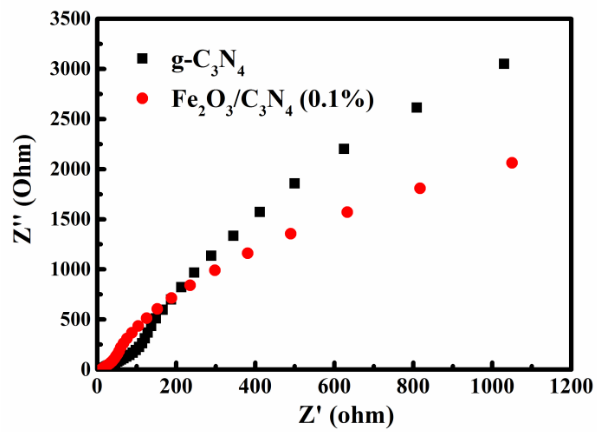

Fig. S3. EIS of FTO/g-C_3N_4 and FTO/Fe(Ⅲ)/g-C_3N_4 (0.1%) electrodes with an applied bias potential of 0.5 V (color online)

The EIS technique is widely used to investigate the charge transfer rate at semiconductor/electrolyte interfaces.

References

[1] Y. Y. Zhong, G. Zhao, F. K. Ma, Y. Z. Wu, X. P. Hao, Appl. Catal. B **199**, 466 (2016).

[2] M. Nishikawa, S. Yuto, T. Hasegawa, W. Shiroishi, H. Honghao, Y. Nakabayashi, Y. Nosaka, N. Saito, Mater. Sci. Semicond. Process **57**, 12 (2017).

[3] P. Zhang, X. X. Teng, X. H. Feng, S. M. Ding, G. Q. Zhang, Ceram. Int. **42**, 16749 (2016).

[4] H. H. Li, X. Y. Wu, S. Yin, K. Katsumata, Y. H. Wang, Appl. Surf. Sci. **392**, 531 (2017).

[5] P. W. Koha, M. H. M. Hattaa, S. T. Ong, L. Yuliati, S. L. Lee, J. Photochem. Photobiol. A **332**, 215 (2017).

[6] Q. Sun, P. Wang, H. G. Yu, X. F. Wang, J. Mol. Catal. A: Chem. **424**, 369 (2016).

[7] S. H. Xun, Z. Y. Zhang, T. Y. Wang. D. L. Jiang, H. M. Li, J. Alloys Compd. **685**, 647 (2016).

[8] X. Zhao, X. Liu, M. M. Yu, C. Wang, J. Li, Dyes and Pigments **136**, 648 (2017).

[9] X. J. Wang, J. K. Song, J. Y. Huang, J. Zhang, X. Wang, R. R. Ma, J. Y. Wang, J. F. Zhao, Appl. Surf. Sci. **390**, 190 (2016).

[10] D. Wang, X. Li, J. Chen, X. Tao, Chem. Eng. J. **198-199**, 547 (2012).

[11] X. C. Wang, K. Maeda, A. Thomas, K. Takanabe, G. Xin, J. M. Carlsson, K. Domen, M. Antonietti, Nature Mater. **8**, 76 (2009).

[12] S. C. Yan, Z. S. Li, Z. G. Zou, Langmuir **25**, 10397 (2009).

[13] J. Wen, J. Xie, X. Chen, X. Li, Appl. Surf. Sci. **391**, 72 (2017).

[14] A. Nikokavoura, C. Trapalis, Appl. Surf. Sci. **430**, 18 (2018).

[15] G. Zhang, C. Huang, X. Wang, Small **11**, 1215 (2015).

[16] P. Wen, P. W. Gong, J. F. Sun, J. Q. Wang, S. R. Yang, J. Mater. Chem. A **3**, 13874 (2015).

[17] D. S. Wang, Z. X. Xu, Q. Z. Luo, X. Y. Li, J. An, R. Yin, C. Bao, J. Mater. Sci. **51**, 893 (2016).

[18] H. F. Shi, G. Q. Chen, C. L. Zhang, Z. G. Zou, ACS Catal. **4**, 3637 (2014).

[19] J. Wang, P. Guo, M. F. Dou, J. Wang, Y. J. Cheng, P. G. Jonsson, Z. Zhao, RSC Adv. **4**, 51008 (2014).

[20] H. Xu, Y. X. Song, Y. H. Song, J. X. Zhu, T. T. Zhu, C. B. Liu, D. X.Zhao, Q. Zhang, H. M. Li, RSC Adv. **4**, 34539 (2014).

[21] S. Samanta, S. Martha, K. Parida, Chem. Cat. Chem. **6**, 1453 (2014).

[22] X. J. Bai, R. L. Zong, C. X. Li, D. Liu, Y. F. Liu, Y. F. Zhu, Appl. Catal. B **147**, 82 (2014).

[23] E. Z. Liu, J. Fan, X. Y. Hu, Y. Hu, H. Li, C. N. Tang, L. Sun, J. Wan, J. Mater. Sci. **50**, 2298 (2015).

[24] Y. P. Li, F. T. Li, X. J. Wang, J. Zhao, J. N. Wei, Y. J. Hao, Y. Liu, Int. J. Hydrogen Energ. **42**, 28327 (2017).

[25] S. Bandaru, G. Saranya, W, W. Liu, N. J. English, Catal. Sci. Technol. **10**, 1376 (2020).

[26] B. R. Duan, L. Mei, J. Colloid Interf. Sci. **575**, 265 (2020).

[27] Y. C. Zhang, Q. Zhang, Q. W. Shi, Z. Y. Cai, Z. J. Yang, Sep. Purif. Technol. **142**, 251 (2015).

[28] H. T. Wei, Q. Zhang, Y. C. Zhang, Z. J. Yang, A. P. Zhu, D. D. Dionysiou, Appl. Catal. A **521**, 9 (2016).

[29] D. S. Wang, H. T. Sun, Q. Z. Luo, X. L. Yang, R. Yin, Appl. Catal.,B **156-157**, 323 (2014).
[30] L. Ge, C. C. Han, J. Liu, J. Mater. Chem. **22**, 11843 (2012).
[31] X. Wang, K, Wang, K, Feng, F. Chen, H. Yu, J. Yu, J. Mol. Catal. A: Chem. **391**, 92 (2014).
[32] H. Yu, G. Cao, F. Chen, X. Wang, J. Yu, M. Lei, Appl. Catal. B **160-161**, 658 (2014).
[33] H. Yu, L. Xu, P. Wang, X. Wang, J. Yu, Appl. Catal. B **144**, 75 (2014).
[34] X. Y. Li, D. Wu, Q. Z. Luo, J. An, R. Yin, D. S. Wang, J. Mater. Sci. **52**, 736 (2017).
[35] R. Yin, Q. Z. Luo, D. S. Wang, H. T. Sun, Y. Y. Li, X. Y. Li, J. An, J. Mater. Sci. **49**, 6067 (2014).
[36] X. Y. Li, D. Wu, Q. Z. Luo, R. Yin, J. An, S. J. Liu, D. S. Wang, J. Alloys Compd. **702**, 585 (2017).
[37] Y. Wang, X. C. Wang, M. Antonietti, Angew. Chem. Int. Ed. **51**, 68 (2012).
[38] G. Z. Liao, S. Chen, X. Quan, H. Yu, H. Zhao, J. Mater. Chem. **22**, 2721 (2012).
[39] B. R. Zeng, L. C. Zhang, X. Y. Wan, H. J. Song, Y. Lv. Sens. Actuators, B **211**, 370 (2015).
[40] K. C. Christoforidis, T. Montini, E. Bontempi, S. Zafeiratos, J. J. D. Jaen, P. Fornasiero, Appl. Catal. B **187**, 171 (2016).
[41] A. Andreyev, M. Akaishi, D. Golberg, Diamond Relat. Mater. **11**, 1885 (2002).
[42] X. Dai, X. M. Lie, S. G. Meng, X. L. Fu, S. F. Chen, Appl. Catal. B **158**, 382 (2014).
[43] F. Jiang, T. T. Yan, H. Chen, A. W. Sun, C. M. Xu, X. Wang. Appl. Surf. Sci. **295**, 164 (2014).
[44] G. Li, K. H. Wong, X. Zhang, C. Hu, J. C. Yu, R. C. Y. Chan, P. K. Wong, Chemosphere **76**, 1185 (2009).
[45] J. S. Cho, Y. J. Hong, Y. C. Kang, ACS Nano **9**, 4026 (2015).
[46] J. N. Zhang, K. X. Wang, Q. Xu, Y. C. Zhou, F. Y. Cheng, S. J. Guo, ACS Nano **9**, 3369 (2015).
[47] F. Tian, Y. Zhang, J. Zhang, C. Pan, J. Phys. Chem. C **116**, 7515 (2012).
[48] Y. Liu, Y. X. Yu, W. D. Zhang, Int. J. Hydrog. Energy **39**, 9105 (2014).
[49] Y. Zhao, C. Eley, J. P. Hu, J. S. Foord, L. Ye, H. Y. He, S. C. E. Tsang, Angew. Chem. Int. Ed. **51**, 3846 (2012).
[50] F. Chang, Y. C. Xie, C. L. Li, J. Chen, J. R. Luo, X. F. Hu, J. W. Shen, Appl. Surf. Sci. **280**, 967 (2013).
[51] Q. Z. Luo, L. Wang, D. S. Wang, R. Yin, X. Y. Li, J. An, X. L. Yang, J. Environ. Chem. Eng. **3**, 622 (2015).
[52] J. P. Wang, C. Q. Li, J. K. Cong, Z. W. Liu, H. Z. Zhang, M. Liang, J. K. Gao, S. L. Wang, J. M. Yao, J. Solid State Chem. **238**, 246 (2016).

*Corresponding author: dswang06@126.com; wangdesong@hebust.edu.cn